Wu *et al. Energy Mater* 2024;4:400015
DOI: 10.20517/energymater.2023.75

Energy Materials

Article

Open Access

Check for updates

Metal- and binder-free dual-ion battery based on green synthetic nano-embroidered spherical organic anode and pure ionic liquid electrolyte

Hongzheng Wu[1,2], Shenghao Luo[1,2], Wen Zheng[3], Li Li[3], Yaobing Fang[2], Wenhui Yuan[1,2,*]

[1]School of Chemistry and Chemical Engineering, South China University of Technology, Guangzhou 510640, Guangdong, China.
[2]Guangdong Engineering Technology Research Centre of Advanced Insulating Coating, South China University of Technology-Zhuhai Institute of Modern Industrial Innovation, Zhuhai 519175, Guangdong, China.
[3]School of Environment and Energy, South China University of Technology, Guangzhou 510640, Guangdong, China.

***Correspondence to:** Prof. Wenhui Yuan, School of Chemistry and Chemical Engineering, South China University of Technology, 381 Wushan Road, Tianhe District, Guangzhou 510640, Guangdong, China. E-mail: cewhyuan@scut.edu.cn

How to cite this article: Wu H, Luo S, Zheng W, Li L, Fang Y, Yuan W. Metal- and binder-free dual-ion battery based on green synthetic nano-embroidered spherical organic anode and pure ionic liquid electrolyte. *Energy Mater* 2024;4:400015. https://dx.doi.org/10.20517/energymater.2023.75

Received: 19 Sep 2023 **First Decision:** 9 Nov 2023 **Revised:** 29 Nov 2023 **Accepted:** 12 Dec 2023 **Published:** 27 Feb 2024

Academic Editors: Yuping Wu, Giovanni B. Appetecchi **Copy Editor:** Fangling Lan **Production Editor:** Fangling Lan

Abstract

Dual-ion batteries (DIBs) have attracted extensive attention and investigations due to their inherent wide operating voltage and environmental friendliness. Nevertheless, the vast majority of DIBs employ metal-based anode active materials or electrolytes, which are relatively costly and unsustainable. Moreover, the utilization of binders and current collectors in the preparation of cathodes and anodes reduces the energy density to a certain extent, which weakens the advantages of DIBs. Here, we synthesized three types of binder-free nano-embroidered spherical polyimide anode materials composed entirely of renewable elements, paired with pure ionic liquid electrolyte without metal elements and flexible self-supporting independent graphite paper cathode without current collector, to construct a class of totally metal and binder-free DIBs. It significantly improves specific discharge capacity, energy density, cyclic stability, and fast charging performance while remarkably reducing costs and self-discharge rate. Additionally, we overcame the drawbacks of conventional synthesis methods and innovatively prepared nanoscale polyimide materials by a green and facile hydrothermal method, which effectively minimizes synthesis costs and avoids risks. This novel battery system design strategy will promote the advancement of low-cost, high-performance DIBs and could be a promising candidate for large-scale energy storage applications.

Keywords: Metal- and binder-free, ionic liquid, polyimide nano-anode, graphite paper, high performance

INTRODUCTION

The high energy density, long cyclic life, and no memory effect of lithium-ion batteries (LIBs) enable them to occupy a major share of the electrochemical energy storage (EES) market since their commercialization and are widely used in portable electronic devices and electric vehicles[1-4]. However, the scarcity and uneven distribution of metal resources, such as lithium and cobalt, drive up the manufacturing and usage costs of LIBs year by year, rendering it difficult to achieve large-scale grid-level energy storage applications. Against such a background, there is an urgent requirement to develop novel battery systems to meet the imminent demand for green and sustainable energy storage programs[5-8]. Different from LIBs, dual-ion batteries (DIBs) allow the simultaneous participation of anions and cations in the electrochemical reaction during charging and discharging, and electrolyte is the singular source of active ions[9-12]. Additionally, inexpensive graphite can be employed to avoid the use of expensive transition metal-based materials as the cathode. This unique reaction mechanism endows DIBs with high cost-effectiveness, suitable operating voltage, and environmental friendliness, which have continuously attracted great interest and research enthusiasm from researchers in recent years[13-15].

Currently, the anode of DIBs is mainly based on inorganic materials such as carbonaceous materials[16-18], alloy-based materials[19-21] and transition metal-based compounds[22-24], which are based on intercalation, alloying, and transformation reactions to accomplish the storage of active ions, respectively. Unfortunately, DIBs based on these electrodes usually undergo structural exfoliation and volume expansion during cycling, causing poor stability, low specific discharge capacity (SDC), and a reduced initial Coulomb efficiency (ICE). In particular, this is not in line with the development concept of "green and sustainable batteries"[25,26]. The key technology for green, sustainable DIBs is the exploration of organic anode materials composed entirely of renewable elements from nature. Organic materials are considered as excellent candidates for the next generation of green and sustainable EES due to their inherent merits of being metal-free and widely available, eco-friendly, cost-effective, and structurally well-designed[27-33]. However, an understanding of their application in DIBs is still in its infancy. Several organic materials have been reported, such as polycyclic aromatic hydrocarbon[34,35], nitrogen/sulfur-containing organics[36,37], carbonyl compounds[38,39], and so on. Organic carbonyl compounds are of great research fascination owing to their simplified synthetic route, unique multi-electron reaction, and structural diversity[40]. Unfortunately, small molecule carbonyl compounds inevitably dissolve in organic electrolytes, leading to terrible cyclic stability and accelerated capacity degradation, limiting their application in large-scale energy storage. Numerous attempts have been made by investigators to avoid dissolution and achieve excellent electrochemical performance. Due to their composition of organic cations and inorganic anions, ionic liquids have a broad electrochemical window. They are kinetically stable, free of solvent molecules, and non-flammable. Therefore, a feasible alternative is to adopt ionic liquids instead of traditional organic solvents[41-43]. Particularly, ionic liquids operate both as solvents and as active ions participating in electrochemical reactions, not only effectively preventing dissolution but also avoiding the use of electrolyte metal salts. Another feasible approach is to design organic polymers with stable inactive backbones and highly redox-active carbonyl functional groups such as polyimide (PI) electrode materials[44]. Additionally, employing nano-engineering design strategies can further increase the active sites of electrode materials and facilitate the transport of active ions and electrolyte penetration, which is beneficial for improving the SDC and electrode reaction kinetics[45,46]. Nevertheless, the application of PI as anodes for DIBs has rarely been reported. One of the main challenges is the dilemma of synthesis, followed by a long (> 8 h) polycondensation reaction at high temperatures (> 200 °C) under a catalyst and N_2 atmosphere, and the final product also needs to be baked in a tube furnace at high temperatures (> 300 °C) for more than 8 h to remove the solvent[47,48]. As a consequence, the whole procedure is time-consuming and costly, with certain technical challenges and safety risks. In this regard, it is essential to explore a cost-effective, energy-saving,

green, and safe synthesis path to obtain comparable or even superior performance.

Herein, after continuous trial and exploration, we have developed a simplified one-step green synthesis strategy, and three types of PI nano-anode materials can be obtained directly by hydrothermal reactions at 160 °C for 6 h. Besides, the straightforward adoption of independent graphite paper (GP) with self-supporting capability as the cathode and current collector, and the anode is binder-free, which greatly improves the discharge capacity and energy density. Combined with a pure ionic liquid electrolyte, a dual-ion full battery system without metal elements and binder is constructed. The reaction principle of the electrodes and the working mechanism of the battery are investigated through a series of physical and chemical characterizations. Such innovative DIBs with outstanding electrochemical performance furnish insight into the establishment of greener and sustainable EES systems and are expected to be applied in large-scale energy storage.

EXPERIMENTAL

Materials

Pyromellitic anhydride, o/m/p-phenylenediamine (o/m/p-PDA), N-methylpyrrolidone (NMP), and GP were purchased from Macklin. Glass fiber diaphragm (GF/A), conductive agent (Super P), carbon-coated aluminum foil, and CR2025 type cell shells were purchased from Clorod. N-butyl-N-methylpyrrolidinium bis(trifluoromethanesulfonyl)imide ionic liquid was purchased from Lanzhou Institute of Chemical Physics, Chinese Academy of Sciences. Unless otherwise stated, no further treatment was required for all materials.

Synthesis of o-PDI, m-PDI, and p-PDI

Firstly, homophthalic anhydride and o/m/p-PDA are added sequentially to 110 mL of deionized water in a 1:3 molar ratio and stirred overnight at room temperature on a magnetic stirrer, then poured into a reaction kettle equipped with 250 mL PTFE liner and finally reacted hydrothermally in an oven at 160 °C for 6 h. After cooling to room temperature, the reaction was filtered with water, methanol, and ethanol successively and dried in a freeze dryer for 48 h. The as-prepared samples were named as o-PDI, m-PDI, and p-PDI.

Materials characterizations

Scanning electron microscopy (SEM) images and energy-dispersive X-ray spectroscopy (EDX) spectra and corresponding mappings were acquired on a scanning electron microscope (Merlin, ZEISS, Germany). X-ray diffraction (XRD) patterns were collected on a D8 Advance X-ray diffractometer (Bruker, Germany) with Cu Kα radiation (λ = 1.5406 Å). Raman spectra were collected on a WITec Apyron micro-Raman spectrometer (WITec, Germany) using a 532 nm laser with a frequency range from 400 to 4,000 cm^{-1}. The Brunauer-Emmett-Teller (BET) surface area and N_2 physical adsorption-desorption analysis were conducted on the Micromeritics ASAP2460 analyzer, USA. The X-ray photoelectron spectroscopy (XPS, Al-Kα radiation, hν = 1,486.6 eV) was used to test the chemical composition of the o/m/p-PDI and the electrodes. Fourier Transform Infrared Spectroscopy (FT-IR) spectrometry (Perkin Elmer Frontier) was used to study the variation of functional groups of organics. Thermogravimetric analysis (TGA, NETZSCH 209F1) was conducted from 25 to 800 °C at a heating rate of 5 °C min^{-1} in N_2.

Battery assembly and measurements

In order to evaluate the electrochemical performance of the dual ion battery, the full battery was assembled by using CR-2025 type button cells in a super glove box (H_2O < 0.01 ppm, O_2 < 0.01 ppm), in which the cathode is directly employed with independent GP with self-supporting capability. As for the preparation of the anode, o/m/p-PDI and Super P are mixed in the ratio of 6:4 and added to a weighing bottle containing NMP without any binder added. Magnetic stirring was done overnight to form a homogeneous slurry, which was later coated on top of the carbon-coated aluminum foil with a coating thickness of 100 μm. The

coating is then transferred to a vacuum drying oven at 100 °C for 12 h. Both the cathode and anode are cut into 14 mm diameter discs and placed in a glove box for use. The mass loading of the anode is ~0.7 mg cm^{-2}, and the SDC/energy density of the DIB is calculated based on the anode. Galvanostatic charge-discharge (GCD)/rate/self-discharge/fast charging-slow discharging performance measurements were carried out using the Neware battery test system. Cyclic voltammetry (CV) and electrochemical impedance spectroscopy (EIS) measurements were performed by using CHI660E and Gamry electrochemical workstations.

RESULTS AND DISCUSSION

Physical characterizations

As shown in Supplementary Schematic 1, three types of PI materials (o-PDI, m-PDI, and p-PDI) were synthesized by using three phenylenediamine isomers (o/m/p-PDA) and pyromellitic dianhydride (PMDA) through a green hydrothermal polycondensation reaction and freeze-drying. Figure 1A-C presents the SEM of the as-prepared o-PDI, m-PDI, and p-PDI, respectively, which all exhibit an embroidered spherical morphology. The elemental mapping in Figure 1D and Supplementary Figures 1 and 2 shows that the C, N, and O elements are uniformly distributed. Specifically, each hydrangea is composed of nanoscale flakes with thicknesses between 10~20 nm and displays a three-dimensional porous network interleaved structure. This distinctive nano-morphology configuration facilitates adequate electrolyte infiltration, diffusion, and storage of active ions, thus improving the ion transport kinetics, rate capability, and discharge capacity. Besides, o-PDI and p-PDI exhibit a tight build-up of some lamellae, mainly due to the spatial site resistance limitation by the formation of cyclic imides between the carbonyl group and two amine groups[49-52]. It is noteworthy that m-PDI is homogeneously dispersed, which plays a role in the reaction kinetics when acting as anode. Meanwhile, the chemical structures of o-PDI, m-PDI, and p-PDI were characterized by FT-IR, XRD, and XPS. The characteristic peaks from the benzene ring structure and the stretching vibration peaks of C=O and C-N bonds on the cyclic imide groups are located within the regions of 680~900, 1,320~1,780, and 3,280~3,520 cm^{-1}, as shown in Figure 1E[44,53]. The Powder XRD patterns in Figure 1F indicate that all three PIs possess crystalline domains and well-defined crystallinity. The chemical compositions of o-PDI, m-PDI, and p-PDI were further elucidated by XPS. The characteristic peaks at ~284, 400, and 531 eV in the full XPS survey spectrum belong to C 1s, N 1s, and O 1s, respectively [Figure 1G], and no additional impurity peaks were observed, indicating high purity. Three different components are demonstrated in the fitted high-resolution C 1s spectrum [Figure 1H and Supplementary Figure 3], attributed to sp^2 C, C-N/C=O, and imide groups[54,55]. Similarly, the characteristic peaks of C-N and aromatic imide N are included in the fitted high-resolution N 1s spectrum [Figure 1I and Supplementary Figure 4], and the peaks ascribed to C=O and O=C-N are included in the fitted high-resolution O 1s spectra [Figure 1J and Supplementary Figure 5][56-58]. In addition, as shown in Supplementary Table 1, it is clear from the XPS-mapping results that the C, N, and O elemental ratios of o-PDI, m-PDI, and p-PDI are close to each other, with minor differences. The above characterization results strongly confirm the successful synthesis of high-purity o-PDI, m-PDI, and p-PDI.

The structural stability of the materials was investigated via the dissolution of the electrode sheets in electrolyte and TGA, respectively. The Pyr_{14}TFSI ionic liquid electrolyte placed with PMDA, o-PDI, m-PDI, and p-PDI electrode sheets, respectively, showed no variations with time migration and remained clear and transparent even after one month [Supplementary Figure 6], indicating that o-PDI/m-PDI/p-PDI exhibits excellent stability in this ionic liquid. This is supported by the TGA curves in Figure 1K, where the three phenylenediamine isomers decomposed at ~150 °C with significant mass loss, and the PMDA monomer also decomposed at around ~250 °C with poor stability. On the contrary, the stability of o/m/p-PDI increased noticeably, with the onset decomposition temperature of o-PDI and p-PDI reaching up to ~425 °C. Surprisingly, m-PDI shows the most outstanding stability with a decomposition temperature of

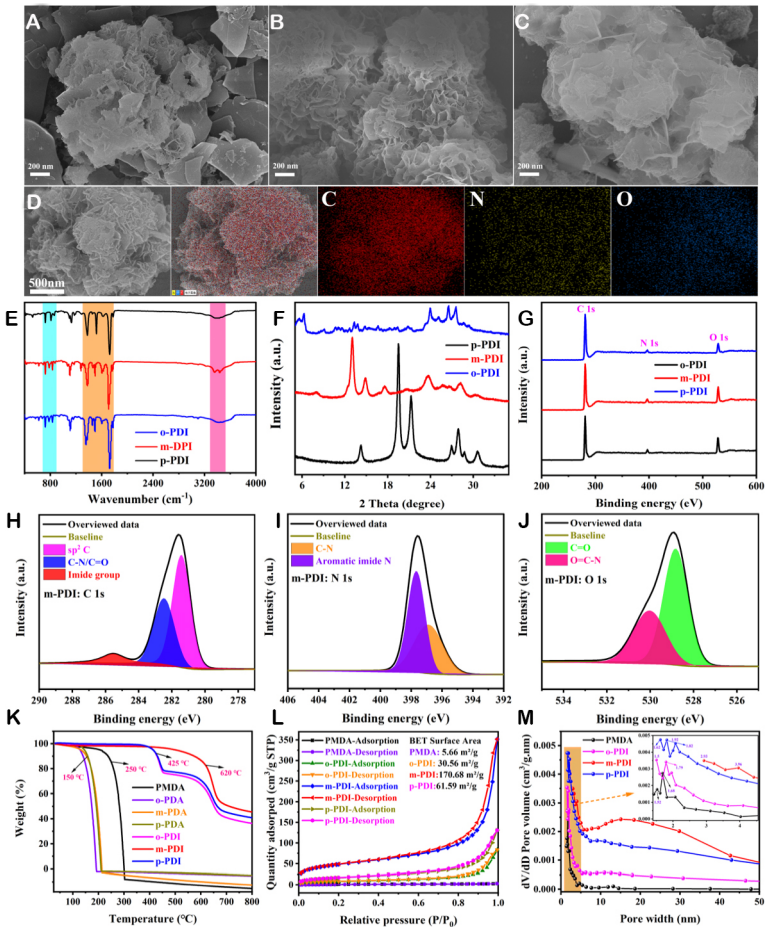

Figure 1. Characterizations of the o-PDI, m-PDI, and p-PDI. (A-C) SEM. (D) Elemental analysis. (E) FT-IR. (F) XRD. (G-J) XPS. (K) TGA. (L and M) N_2 adsorption/desorption curves and pore size distributions.

620 °C. The specific surface area and porous properties of PMDA and o-PDI/m-PDI/p-PDI are characterized by N_2 adsorption/desorption isotherms and pore size distribution, which exhibit typical type IV isotherms [Figure 1L][59,60], as PMDA possesses the lowest BET surface area of 5.66 m^2/g, while o-PDI and p-PDI increased to 30.56 and 61.59 m^2/g, respectively. Particularly, m-PDI displays the largest specific surface area of 170.68 m^2/g, which is more favorable for enhancing the effective contact area with electrolytes and providing more surface and space for charge diffusion and active ion storage. The pore size distributions of PMDA, o-PDI, and p-PDI are distributed between 1 and 2 nm based on the Barrett-Joyner-Halenda method [Figure 1M] and are dominated by microporous structures. In contrast, the pore size distribution of m-PDI ranges from 3 to 30 nm with predominantly mesoporous structures, which are more conducive to facilitating electron/ion transport and delivering more active sites.

Electrochemical performance and kinetics of o-PDI, m-PDI, and p-PDI

A $Pyr_{14}TFSI$ ionic liquid electrolyte-based button-type battery was used to probe the active ion storage capacity and reaction kinetics of the electrodes. Supplementary Figure 7 shows the two-electrode cyclic voltametric (CV) curves based on PMDA electrodes at different cycles scanned from the open circuit voltage in the negative direction at a rate of 1 mV/s. No redox peaks appear, indicating that no electrochemical redox reaction occurs and the PMDA electrode cannot store active ions[61,62]. Interestingly, when replaced with the o-PDI/m-PDI/p-PDI electrode, two pairs of sharp redox peaks emerge, as shown in

Figure 2A-C, respectively, and all the CV curves overlap, indicating excellent cycling reversibility and stability. Figure 2D and Supplementary Figure 8A-C depict the GCD curves based on PMDA, o-PDI, p-PDI, and m-PDI anodes, respectively. The full battery system, on the basis of PMDA anodes, exhibits two inclined curves without charge/discharge plateaus [Supplementary Figure 8A]. In contrast, the systems based on m-PDI, o-PDI, and p-PDI anodes all display typical active ion insertion/de-insertion behavior with two pairs of symmetrical charge/discharge plateaus [Figure 2D and Supplementary Figure 8B and C], respectively, in accordance with the CV curves. Similar to the GCD curves, the dQ/dV curves in Supplementary Figure 9 indicate that the charging and discharging processes of o-PDI, p-PDI, and m-PDI are divided into two regions except for PMDA, which represent the various stages of insertion and de-insertion, respectively[63-65]. The electrochemical storage behavior and reaction kinetics of o-PDI, m-PDI, and p-PDI were further analyzed by CV curves at different scan rates (0.2/0.4/0.6/0.8/1 mV/s), and the results are summarized in Figure 2E and Supplementary Figure 10A and B. All of the CV curves manifest an analogous silhouette and well-defined redox peaks, which indicate a stable electrochemical performance[23,66]. The voltammetric response of the electrode at various scan rates can be quantified based on the power-law relationship ($i = av^b$) concerning the redox peak current i and the scan rate v, where b is a constant and a *b* value of 0.5 indicates that the electrochemical reaction is an ideal diffusion-controlled process, while a *b* value of 1.0 represents that the energy storage process is surface capacitance-controlled[67-69]. It is evident from Figure 2F and Supplementary Figure 11A and B that the *b*-values of o-PDI, m-PDI, and p-PDI electrodes based on redox peaks are all in the range of 0.5-1.0 with the *b*-value of m-PDI being closest to 1, indicating that the electrode reaction kinetics are synergistic by diffusion and capacitive reactions.

Quantitatively, the capacitive contribution is calculated based on Dunn's method: $i = k_1v + k_2v^{1/2}$, where k_1 and k_2 are constants, and k_1v and $k_2v^{1/2}$ represent the pseudocapacitance contribution and the diffusion contribution, respectively. Consequently, the pseudocapacitance contributions of o-PDI, m-PDI, and p-PDI electrodes at 1 mV/s are 0.69, 0.95, and 0.89 (the red-filled part in Figure 2G and Supplementary Figure 12A and B), respectively. As the scan rate increases, the diffusion contribution gradually reduces, and the pseudocapacitance contribution enhances accordingly [Figure 2H and Supplementary Figure 13A and B]. Particularly, m-PDI demonstrates the highest percentage of pseudocapacitance contribution at either rate, which is more favorable for improving the electrode reaction kinetics and rate capability[70-72]. Furthermore, the peak current i is proportional to the square root of the scan rate ($v^{0.5}$), as seen in Figure 2I and Supplementary Figure 14A and B. Therefore, the ion diffusion coefficient for each electrode can be calculated from the Randles-Sevcik equation: $i_p = 269{,}000\ CSD^{1/2}v^{1/2}n^{3/2}$, where C is the electrolyte concentration, S is the electrode surface area, D is the diffusion coefficient, n is the number of electrons transferred, and the value of $i_p/v^{1/2}$ is the slope k[73,74]. Among the o-PDI, m-PDI, and p-PDI electrode systems, the values of C, S, and n are identical, implying that the diffusion coefficient D is only related to the value of k. It can be concluded from Figure 2I and Supplementary Figure 14 that the magnitude of *k* values for all redox peaks corresponding to the three types of PI is m-PDI > p-PDI > o-PDI, which means that the m-PDI electrode endows the maximum ion diffusion coefficient and is more beneficial to promote the ion transport kinetics.

Electrochemical performance of o//G-DIB, m//G-DIB, p//G-DIB

The proof-of-concept full batteries based on o-PDI/m-PDI/p-PDI anodes, GP cathodes, and Pyr_{14}TFSI ionic liquid electrolytes were constructed respectively to further investigate the electrochemical performance for various systems (abbreviated as o//G-DIB, m//G-DIB, p//G-DIB). In particular, GP is a type of conductive carbon material featuring self-supporting flexibility capability without current collectors [Supplementary Figure 15]; high crystallization and defect-free characteristics can be seen from XRD and Raman plots [Supplementary Figures 16 and 17]. Additionally, both the cathode and anode are metal and

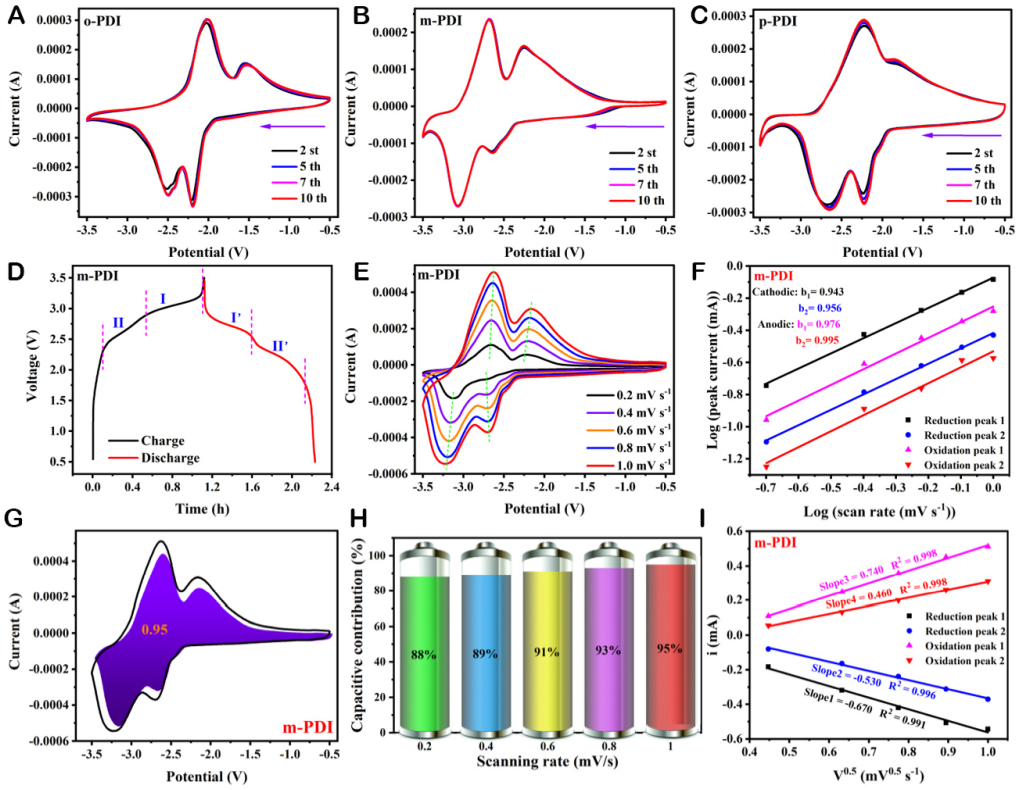

Figure 2. Electrochemical performance and kinetic characterizations of o-PDI, m-PDI, and p-PDI electrodes. (A-C) CV tests at 1 mV/s. (D) GCD curves. (E) CV curves at various scan rates and (F) The corresponding *b* values derived from i = av^b.(G) Pseudocapacitance ratio of m-PDI at 1 mV/s. (H) Contribution of pseudocapacitance at different scan rates. (I) Linear relationship between i and the square root of v.

binder-free, which is beneficial for improving the SDC and energy density, further reducing cost and being in line with the green development concept. Figure 3A-C illustrates the GCD curves of the three battery systems at different rates. With the rate increase, the gap between the charge and discharge plateaus tends to become larger, which is due to the more pronounced polarization at higher current density[75,76]. This is corroborated by the dQ/dV curves in Figure 3D and Supplementary Figure 18, where the oxidation peak gradually shifts to a higher potential and the reduction peak shifts to a lower potential as the current density rises, accompanied by a weakening of the peak intensity. However, the three systems consistently maintain clear charge/discharge plateaus, indicating the fast ion diffusion kinetics. The rate performance of o//G-DIB, m//G-DIB, and p//G-DIB was tested from 0.2 to 10 C (1 C = 100 mA/g). Specifically, o//G-DIB and p//G-DIB delivered reversible SDCs of 144 and 168 mA h g^{-1} at a low rate of 0.2 C, respectively, and still possess SDCs of 61 and 71 mA h g^{-1}, respectively, even at high rate of 10 C [Figure 3E]. Notably, m//G-DIB performs optimally, delivering SDCs up to 222 and 91 mA h g^{-1} at 0.2 C and 10 C, respectively, and providing energy densities up to 409.8 and 221.3 Wh kg^{-1} at 0.2 C based on the anode and total mass, respectively. This is attributed to the fact that the m-PDI anode exhibits the optimized ion transport and storage capability, which can be extrapolated from the Nyquist plots based on EIS in Figure 3F and Supplementary Figure 19; the upper insets are the equivalent circuits used to fit the corresponding EIS plots respectively. Where the arc in the high-frequency region represents the charge transfer impedance Rct and the line sloping in the low-frequency region represents the Warburg impedance with a slope of k, which is related to the diffusion barrier of active ions in the electrode. Compared with o-PDI and p-PDI, the m-PDI electrode displays the smallest value of Rct and decreases after multiple cycles. This may be due to the fact

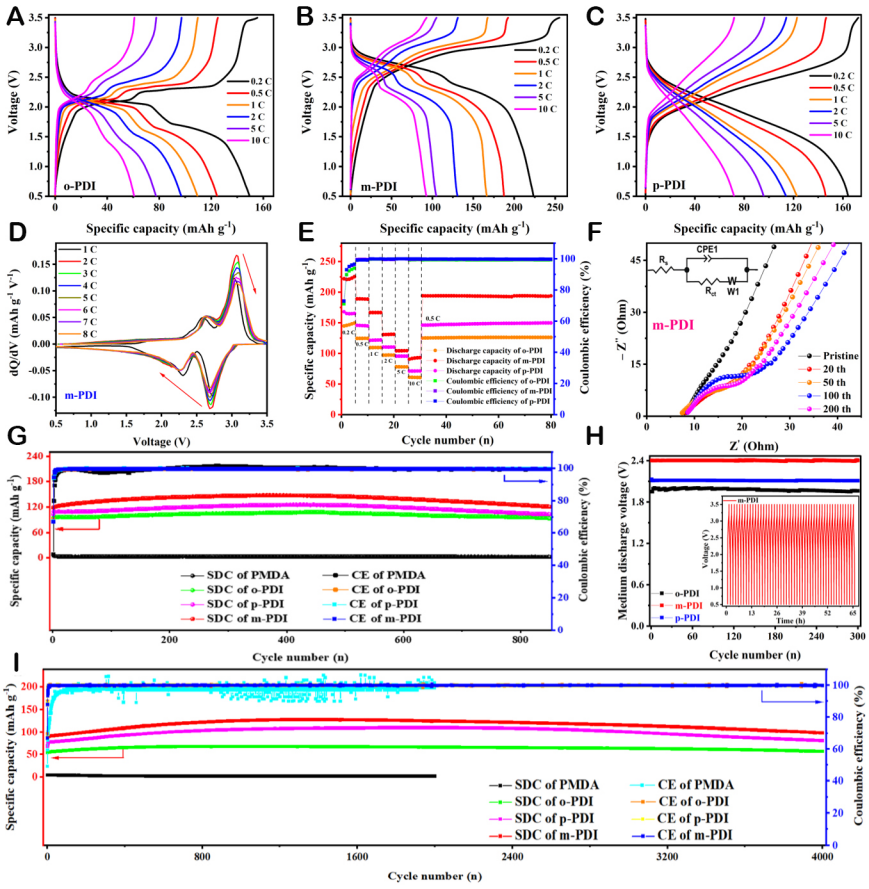

Figure 3. Electrochemical performances of o//G-DIB, m//G-DIB, and p//G-DIB. (A-C) GCD curves at different rates. (D) dQ/dV curves of m//G-DIB. (E) Rate performance. (F) EIS and its fitting diagram. (G) Cyclic performance at 2 C. (H) The medium discharge voltage during cycling. (I) The long-term cyclic performance under 10 C.

that m-PDI possesses the relatively highest specific surface area, which is sufficiently wetted by the electrolyte after cycling. Besides, the m-PDI electrode possesses the largest *k*-value, implying the smallest ion diffusion energy barrier and the fastest ion transport[74,77-79], which is most favorable for the diffusion of active ions, in agreement with the findings in Figure 2G and I. What is remarkable is that when the current density returns to 0.5 C, o//G-DIB, m//G-DIB, and p//G-DIB exhibit higher capacities than the pristine and can be cycled stably, suggesting a high-reversible ion storage capability and excellent rate performance.

The cyclic performance of o//G-DIB, m//G-DIB, and p//G-DIB at 2 C is compared, as shown in Figure 3G, where the reversible initial specific discharge capacities of o//G-DIB and p//G-DIB are 94 and 104 mA h g^{-1}, respectively, and the capacity retentions after 850 cycles are 99% and 99.5%, respectively. Apparently, the m//G-DIB shows the best performance, with an initial SDC (ISDC) of up to 119 mA h g^{-1} and a Coulomb efficiency (CE) of 100%, without capacity degradation after 850 cycles (three months). The full battery system based on PMDA monomer anodes was investigated, with an ISDC of only 7 mA h g^{-1} and a basic loss of capacity after 850 cycles [Figure 3G]. To further exclude the capacity contribution of the conductive agent Super P, its electrochemical performance was studied, as evidenced by the dQ/dV and GCD curves in Supplementary Figures 20 and 21 that there are no redox peaks and charging/discharging plateaus, and it only provides a negligible SDC of 4 mA h g^{-1}. Figure 3H depicts the median voltages of o//G-DIB, m//G-DIB, and p//G-DIB at 5 C. All three systems are extremely stable during cycling with o//G-DIB and

p//G-DIB remaining at 2.0 and 2.1 V, respectively, while m//G-DIB exhibits the maximum of 2.4 V, and the GCD curves (inset in Figure 3H) remain stable, further proving the excellent cyclic stability. Surprisingly, the cyclic stability is superior even at a high rate. As shown in Figure 3I, as the rate rises to 10 C, the o//G-DIB, m//G-DIB, and p//G-DIB deliver ISDCs as high as 54, 68, and 84 mA h g^{-1}, respectively, and can be cycled stably for 4,000 cycles without capacity degradation with CE remaining at 100%. Such outstanding electrochemical performances are superior to those reported so far for dual-ion full battery systems based on organic anodes and pure ionic liquid electrolytes, as shown in Supplementary Table 2.

A low self-discharge rate is an essential performance parameter for full batteries to achieve practical applications, and unfortunately, DIBs are often criticized for exhibiting a comparatively high self-discharge rate. On this basis, the self-discharge performance of o//G-DIB, m//G-DIB, and p//G-DIB was tested separately by fully charging the batteries first and then completely discharging them after 10 h of resting. The results are presented in Figure 4A-F and Supplementary Figure 22, according to the self-discharge rate calculation formula: S = (C - Cr)/CT*100%, where S denotes the self-discharge rate, C and Cr are the SDCs without and after resting, respectively, and T refers to the resting time[23,80]. It can be calculated that the self-discharge rates of o//G-DIB, m//G-DIB, and p//G-DIB are 0.00817, 0.00371 and 0.00603 h^{-1}, respectively, which are significantly lower than the currently reported battery systems, as shown in Supplementary Table 3. Furthermore, researchers are trying to break through the bottleneck of achieving fast charging performance and stable cycling at the same time. For this purpose, the battery is charged at an ultra-high rate of 20 C and then discharged at 1 C to evaluate the cyclic stability. Figure 4G-L demonstrates that the batteries could be fully charged in a maximum of 100 s and are capable of cycling at least 200 cycles without decay. Such excellent fast charging performance and low self-discharge rates enable o//G-DIB, m//G-DIB, and p//G-DIB for large-scale energy storage applications.

Working mechanism and reaction principle

Taking the m//G-DIB system as a typical representative, the unique active ion storage mechanism of cathodes/anodes and the variations of chemical bonds during charging and discharging were investigated by FT-IR, Raman, and XPS. Figure 5A and Supplementary Figure 23 illustrate the FT-IR characterization of the anode under different charging and discharging states. The symmetric and asymmetric stretching vibration peaks of C=O located near 1,742 and 1,769 cm^{-1} basically disappear after being completely charged [Figure 5A], and the characteristic peak of C-O appears near 1,270 cm^{-1} [Supplementary Figure 23]. Meanwhile, it is evident from the fitted high-resolution N1s spectra that N-S and N-F characteristic peaks appeared at 402 and 399 eV, respectively, after completely charged [Figure 5B and Supplementary Figure 24], indicating that C=O is reduced to $C\text{-}O^-$ and undergoes enolization with the inserted Pyr_{14}^+ cations, while the emergence of S 2p and F 1s peaks is attributed to the formation of the solid electrolyte interphase (SEI) by the decomposition of the $TFSI^-$ anions[81-83]. After being fully discharged, the intensities of the C=O and N 1s peaks recover, and the C-O peak disappears, proving the occurrence of a reversible enolization reaction, whereas the S 2p and F 1s peaks are still present with essentially constant intensities, implying the establishment of a stable SEI. With respect to the cathode, the C-F characteristic peak at ~1,334 cm^{-1}, the C-N, C-S, and S=O characteristic peaks between 1,020 and 1,210 cm^{-1} in the FT-IR [Figure 5C], and the S-N-S characteristic peak in the Raman [Figure 5D] emerge after being fully charged[84,85]. Moreover, S 2p, S 2s, N 1s, O 1s, and F 1s peaks appear in the XPS full spectrum [Supplementary Figure 25], strongly demonstrating the intercalation of the $TFSI^-$ anions. The peak signals lie in FT-IR and Raman remarkably reduced but did not vanish after being fully discharged, which might be explained by (1) the residual electrolyte on the electrode sheet; and (2) the formation of stable CEI as the S 2p, S 2s, N 1s, O 1s, and F 1s peaks in Supplementary Figure 25 still possess considerable intensities compared to the fully charged stage.

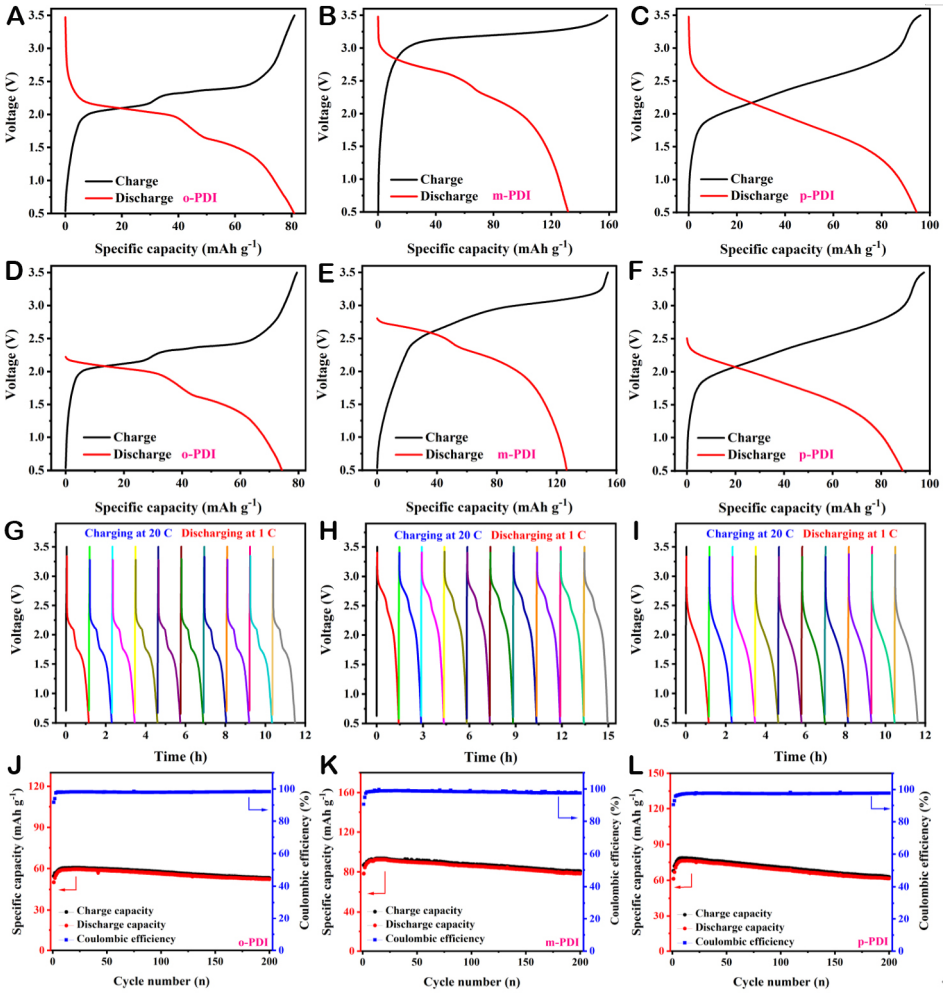

Figure 4. Self-discharge and fast charging performance. GCD curves of (A-C) Unresting and (D-F) Resting for 10 h. (G-I) The first ten cycles of charging at 20 C and discharging at 1 C and (J-L) Corresponding cyclic performance.

From the above characterizations, combined with the CV, dQ/dV, and GCD curves in Figure 2, it can be concluded that the working mechanism of the full battery is depicted in Figure 5E. The electrode reactions involved are shown in (1) to (3): during charging, the active cations and anions in the electrolyte move toward the cathode and anode, respectively, and participate in the electrochemical reactions. Conversely, during the discharge process, the cations and anions return to the electrolyte from the cathode and anode, respectively. Additionally, as shown in Figure 5F, only one coin battery is able to light the LED and successfully charge the smartwatch, indicating a great prospect for practical applications.

Anode: $x(o/m/p\text{ - }PDI)_n + Pyr_{14}^{+} + 2nxe^{-} \leftrightarrow (o/m/p\text{ - }PDI)_{nx}(Pyr_{14})_{2nx}$

Cathode: $yC + 2nxTFSI^{-} \leftrightarrow C_y(TFSI)_{2nx} + 2nxe^{-}$

Overall: $x(o/m/p\text{-}PDI)_n + 2nxPyr_{14}^{+} + yC + 2nxTFSI^{-} \leftrightarrow (o/m/p\text{ - }PDI)_{nx}(Pyr_{14})_{2nx} + C_y(TFSI)_{2nx}$

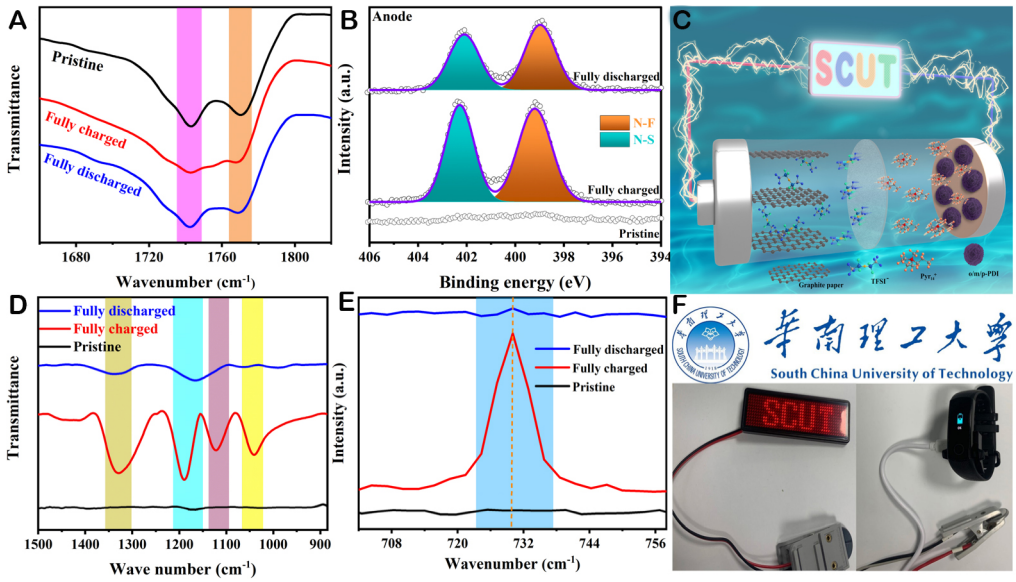

Figure 5. The investigations of energy storage mechanism based on cathodes and anodes. (A) FT-IR and (B) the fitted high-resolution N 1s spectra under pristine, fully charged/discharged state. (C) FT-IR and (D) Raman characterizations of cathodes at different states. (E) The working mechanism of the full battery system. (F) One coin battery is able to light the LED and successfully charge the smartwatch.

Such excellent electrochemical performance is greatly dependent on the superior structural stability of the cathode and anode. To appreciate this, a combination of XRD, Raman, and FT-IR techniques was employed to characterize the electrodes during the charge and discharge process. For the GP cathode, as depicted in Figure 6A and B, the signal of the 002 characteristic peak located at 26.5° decreases gradually during the charging process and drops to a minimum after being completely charged, implying the formation of graphite intercalation compounds (GICs) accompanied by a reduction in crystallinity due to the intercalation of $TFSI^-$[67,75,86]. It can be corroborated by Raman that during the charging process, the graphite layers adjacent to the intercalation layers become highly charged owing to the formation of GICs, and the G peak located at 1,580 cm^{-1} undergoes a blue shift accompanied by a weakening of the signal [Figure 6C and D]; the value of I_G/I_D decreases during charging and reaches a minimum after being fully charged according to Figure 6E and Supplementary Figure 26, indicating an increase of defects and disorder in the graphite layers[87,88]. During the subsequent discharge process, the 002 peak signal gradually strengthens and recovers to the initial value after being fully discharged, confirming the deintercalation of $TFSI^-$. Furthermore, the peak position of the 002 characteristic peak shows no variation throughout the process, and the intensity of the G peak with I_G/I_D value restores during the discharge process, indicating the outstanding structural stability of the GP cathode and the reversible intercalation/deintercalation of $TFSI^-$. Similarly, as for the anode, the intensities of the XRD characteristic peaks located at 14.9° and 20.7° in Figure 6F gradually decrease during the charging process; simultaneously, the carbonyl peaks located at 1,725-1,785 cm^{-1} in Figure 6G disappear progressively, suggesting the ongoing process of the insertion of Pyr_{14}^+ and subsequent enolization reaction[44,57,79]. All the characteristic peaks recover to the initial state during the subsequent discharge process without any shift in peak positions throughout the process, implying a reversible insertion/desertion and enolization reaction. The positions and intensities of the peaks located at ~1,403, 1,504, and 1,591 cm^{-1} attributed to the C-N of imide and the C=C of the benzene ring, respectively, exhibit no variation during the charge and discharge process, demonstrating a well-stabilized structure of the anode. Moreover, Supplementary Figure 27 illustrates the morphology of cathodes and anodes before and after circulation. It can be observed that even after 1,000 cycles, the electrodes still

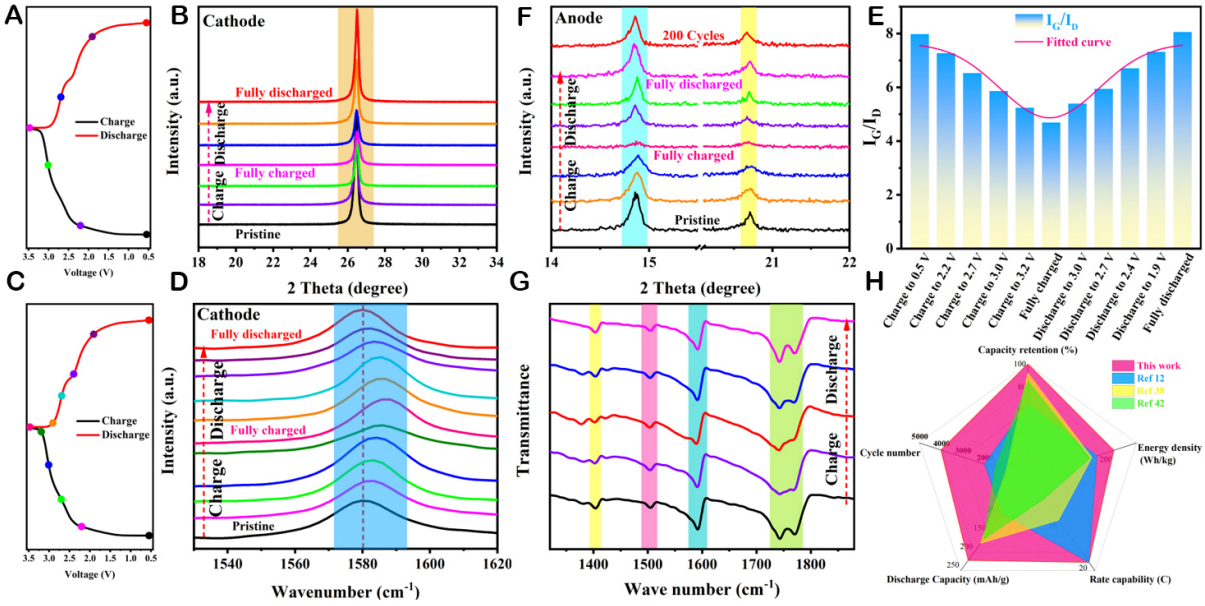

Figure 6. XRD, Raman, and FT-IR characterizations at different charge and discharge states. (A, B, F) XRD and (C, D, G) Raman and FT-IR spectrums of the cathode and anode based on the selected stages. (E) The I_G/I_D values based on different charging and discharging stages. (H) Electrochemical performance comparison of recently reported work in DIBs.

maintain their perfect morphology without damage, further supporting the above conclusion. Remarkably, the achieved performance of the o/m/p-PDI is strongly competitive compared with those recently published works in terms of the capacity retention, energy density, rate capability, discharge capacity, and cycle number, as depicted in Figure 6H, indicating a considerable potential for application in large-scale energy storage applications.

CONCLUSIONS

In summary, three types of PI anode materials with distinctive nano-morphologies, o-PDI, m-PDI, and p-PDI, could be synthesized on a large scale by an innovative green and mild hydrothermal strategy, which breaks through the technical drawbacks of the traditional synthesis of PIs. Through a combination of a series of physicochemical characterizations and electrochemical measurements, it is proved that m-PDI shows the most excellent performance due to the homogeneous and well-dispersed lamellar structure, the maximum specific surface area and pore size, the optimum ion diffusion coefficient, and the highest pseudocapacitance ratio. Matching with the GP cathode with self-supporting flexibility and $Pyr_{14}TFSI$ pure ionic liquid electrolytes, the binder and metal-free o//G-DIB, m//G-DIB, and p//G-DIB full battery systems are constructed, and they exhibit outstanding electrochemical performances: (1) high specific discharge capacities of 144, 222 and 168 mA h g^{-1} at 0.2 C, respectively, and energy densities of 409.8 and 221.3 Wh kg^{-1} based on the anode and total mass; (2) superior rate performance with no capacity degradation for 4,000 cycles at a high rate of 10 C; (3) low self-discharge rates of 0.817, 0.371, and 0.603% h^{-1}, respectively, and superior fast charging performance with a maximum of just 100 s to being fully charged and can be cycled stably. Furthermore, the working mechanism of the full battery and the excellent structural stability of the electrodes have been demonstrated by XPS, FT-IR, XRD, Raman, and SEM, which is expected to inspire the development of the large-scale practical application of environment-friendly DIBs in the future.

DECLARATIONS

Acknowledgments

The authors would like to acknowledge the financial support from the National Natural Science Foundation of China (No. 22075089) and the Fundamental and Applied Fundamental Research Project of Zhuhai City (No. 22017003200023).

Authors' contributions

Prepared the o/m/p-PDI, assembled the dual-ion batteries, and performed most of the electrochemical experiments and physicochemical characterizations: Wu H

Supervised the project: Fang Y, Yuan W

Analyzed the data and co-wrote and discussed the whole paper: Wu H, Luo S, Zheng W, Li L, Fang Y, Yuan W

Availability of data and materials

The data are made available upon request to authors.

Financial support and sponsorship

This work was financially supported by the National Natural Science Foundation of China (No. 22075089) and the Fundamental and Applied Fundamental Research Project of Zhuhai City (No. 22017003200023). The authors would like to thank Jian-ming Liu from the Shiyanjia Lab (www.shiyanjia.com) for the support of SEM, XRD, and Raman testing.

Conflicts of interest

All authors declared that there are no conflicts of interest.

Ethical approval and consent to participate

Not applicable.

Consent for publication

Not applicable.

REFERENCES

1. Li J, Fleetwood J, Hawley WB, Kays W. From materials to cell: state-of-the-art and prospective technologies for lithium-ion battery electrode processing. *Chem Rev* 2022;122:903-56. DOI PubMed
2. Zhang H, Wang L, He X. Trends in a study on thermal runaway mechanism of lithium-ion battery with $LiNi_xMn_yCo_{1-x-y}O_2$ cathode materials. *Battery Energy* 2022;1:20210011. DOI
3. Neumann J, Petranikova M, Meeus M, et al. Recycling of lithium-ion batteries - current state of the art, circular economy, and next generation recycling. *Adv Energy Mater* 2022;12:2102917. DOI
4. Wang E, Xiao D, Wu T, et al. Stabilizing oxygen by high-valance element doping for high-performance Li-rich layered oxides. *Battery Energy* 2023;2:20220030. DOI
5. Du K, Ang EH, Wu X, Liu Y. Progresses in sustainable recycling technology of spent lithium-ion batteries. *Energy Environ Mater* 2022;5:1012-36. DOI
6. Gao C, Jiang Z, Qi S, et al. Metal-organic framework glass anode with an exceptional cycling-induced capacity enhancement for lithium-ion batteries. *Adv Mater* 2022;34:e2110048. DOI
7. Liu Y, Russo PA, Montoro LA, Pinna N. Recent developments in Nb-based oxides with crystallographic shear structures as anode materials for high-rate lithium-ion energy storage. *Battery Energy* 2023;2:20220037. DOI
8. Lee MJ, Han J, Lee K, et al. Elastomeric electrolytes for high-energy solid-state lithium batteries. *Nature* 2022;601:217-22. DOI
9. Ji B, Zhang F, Song X, Tang Y. A novel potassium-ion-based dual-ion battery. *Adv Mater* 2017;29:201700519. DOI

10. Wu X, Xu Y, Zhang C, et al. Reverse dual-ion battery via a $ZnCl_2$ water-in-salt electrolyte. *J Am Chem Soc* 2019;141:6338-44. DOI
11. Zhang X, Tang Y, Zhang F, Lee CS. A novel aluminum-graphite dual-ion battery. *Adv Energy Mater* 2016;6:1502588. DOI
12. Li Y, Wang B. High rate and ultralong cyclelife fiber-shaped sodium dual-ion battery based on bismuth anodes and polytriphenylamine cathodes. *Battery Energy* 2023;2:20220035. DOI
13. Wei B, Hong Y, Tang W, et al. Design of bipolar polymer electrodes for symmetric Li-dual-ion batteries. *Chem Eng J* 2023;451:138773. DOI
14. Das S, Manna SS, Pathak B. Recent advancements in devising computational strategies for dual-ion batteries. *ChemSusChem* 2023;16:e202201405. DOI PubMed
15. Yu M, Liu H, Xiao K, Xie B, Han Z, Wang DW. Redox-mediated proton transport of two-dimensional polyaniline-based nanochannels for fast capacitive performance. *Battery Energy* 2022;1:20210004. DOI
16. Feng Y, Chen S, Wang J, Lu B. Carbon foam with microporous structure for high performance symmetric potassium dual-ion capacitor. *J Energy Chem* 2020;43:129-38. DOI
17. Rothermel S, Meister P, Schmuelling G, et al. Dual-graphite cells based on the reversible intercalation of bis(trifluoromethanesulfonyl)imide anions from an ionic liquid electrolyte. *Energy Environ Sci* 2014;7:3412-23. DOI
18. Wang G, Yu M, Feng X. Carbon materials for ion-intercalation involved rechargeable battery technologies. *Chem Soc Rev* 2021;50:2388-443. DOI
19. Ou X, Li J, Tong X, Zhang G, Tang Y. Highly concentrated and nonflammable electrolyte for high energy density K-based dual-ion battery. *ACS Appl Energy Mater* 2020;3:10202-8. DOI
20. Sheng M, Zhang F, Ji B, Tong X, Tang Y. A novel tin-graphite dual-ion battery based on sodium-ion electrolyte with high energy density. *Adv Energy Mater* 2017;7:1601963. DOI
21. Bizuneh GG, Adam AMM, Ma J. Progress on carbon for electrochemical capacitors. *Battery Energy* 2023;2:20220021. DOI
22. Salunkhe TT, Kadam AN, Kidanu WG, Lee S, Nguyen TL, Kim IT. A diffusion encouraged core-shell heterostructured Co_3Sn_2@SnO_2 anode towards emerging dual ion batteries with high energy density. *J Mater Chem A* 2021;9:14991-5002. DOI
23. Wu H, Li L, Yuan W. Nano-cubic α-Fe_2O_3 anode for Li^+/Na^+ based dual-ion full battery. *Chem Eng J* 2022;442:136259. DOI
24. Wang X, Qi L, Wang H. Anatase TiO_2 as a Na^+-storage anode active material for dual-ion batteries. *ACS Appl Mater Interfaces* 2019;11:30453-9. DOI
25. Kim J, Kim Y, Yoo J, Kwon G, Ko Y, Kang K. Organic batteries for a greener rechargeable world. *Nat Rev Mater* 2023;8:54-70. DOI
26. Poizot P, Dolhem F. Clean energy new deal for a sustainable world: from non-CO_2 generating energy sources to greener electrochemical storage devices. *Energy Environ Sci* 2011;4:2003-19. DOI
27. Esser B, Dolhem F, Becuwe M, Poizot P, Vlad A, Brandell D. A perspective on organic electrode materials and technologies for next generation batteries. *J Power Sources* 2021;482:228814. DOI
28. Feng RZ, Zhang X, Murugesan V, et al. Reversible ketone hydrogenation and dehydrogenation for aqueous organic redox flow batteries. *Science* 2021;372:836-40. DOI
29. Kim J, Kim H, Lee S, et al. A p-n fusion strategy to design bipolar organic materials for high-energy-density symmetric batteries. *J Mater Chem A* 2021;9:14485-94. DOI
30. Lakraychi AE, Dolhem F, Vlad A, Becuwe M. Organic negative electrode materials for metal-ion and molecular-ion batteries: progress and challenges from a molecular engineering perspective. *Adv Energy Mater* 2021;11:2101562. DOI
31. Nguyen TP, Easley AD, Kang NA, et al. Polypeptide organic radical batteries. *Nature* 2021;593:61-6. DOI
32. Xie J, Lu YC. Towards practical organic batteries. *Nat Mater* 2021;20:581-3. DOI PubMed
33. Zhu W, Huang Y, Jiang B, Xiao R. A metal-free ionic liquid dual-ion battery based on the reversible interaction of 1-butyl-1-methylpyrrolidinium cations with 1,4,5,8-naphthalenetetracarboxylic dianhydride. *J Mol Liq* 2021;339:116789. DOI
34. Dong S, Li Z, Rodríguez-pérez IA, et al. A novel coronene//$Na_2Ti_3O_7$ dual-ion battery. *Nano Energy* 2017;40:233-9. DOI
35. Das S, Bhauriyal P, Pathak B. Polycyclic aromatic hydrocarbons as prospective cathodes for aluminum organic batteries. *J Phys Chem C* 2021;125:49-57. DOI
36. Li Q, Wang H, Wang HG, Si Z, Li C, Bai J. A self-polymerized nitro-substituted conjugated carbonyl compound as high-performance cathode for lithium-organic batteries. *ChemSusChem* 2020;13:2449-56. DOI
37. Kolek M, Otteny F, Schmidt P, et al. Ultra-high cycling stability of poly(vinylphenothiazine) as a battery cathode material resulting from π-π interactions. *Energy Environ Sci* 2017;10:2334-41. DOI
38. Han C, Li H, Li Y, Zhu J, Zhi C. Proton-assisted calcium-ion storage in aromatic organic molecular crystal with coplanar stacked structure. *Nat Commun* 2021;12:2400. DOI PubMed PMC
39. Häupler B, Wild A, Schubert US. Carbonyls: powerful organic materials for secondary batteries. *Adv Energy Mater* 2015;5:1402034. DOI
40. Yang H, Lee J, Cheong JY, et al. Molecular engineering of carbonyl organic electrodes for rechargeable metal-ion batteries: fundamentals, recent advances, and challenges. *Energy Environ Sci* 2021;14:4228-67. DOI
41. Shaplov AS, Marcilla R, Mecerreyes D. Recent advances in innovative polymer electrolytes based on poly(ionic liquid)s. *Electrochim Acta* 2015;175:18-34. DOI
42. Chen Y, Yu D, Liu Z, Xue Z, Mu T. Thermal, chemical, electrochemical, radiolytic and biological stability of ionic liquids and deep eutectic solvents. *New J Chem* 2022;46:17640-68. DOI
43. Wang A, Yuan W, Fan J, Li L. A dual-graphite battery with pure 1-butyl-1-methylpyrrolidinium bis(trifluoromethylsulfonyl) imide as

the electrolyte. *Energy Technol* 2018;6:2172-8. DOI

44. Song Z, Zhan H, Zhou Y. Polyimides: promising energy-storage materials. *Angew Chem Int Ed* 2010;49:8444-8. DOI PubMed
45. Wu H, Wang K, Meng Y, Lu K, Wei Z. An organic cathode material based on a polyimide/CNT nanocomposite for lithium ion batteries. *J Mater Chem A* 2013;1:6366-72. DOI
46. Raj M, Mangalaraja RV, Lee G, Contreras D, Zaghib K, Reddy MV. Large π-conjugated condensed perylene-based aromatic polyimide as organic cathode for lithium-ion batteries. *ACS Appl Energy Mater* 2020;3:6511-24. DOI
47. Jiang B, Kong T, Cai Z, Zhu W, Xiao R. In-situ modification of polyimide anode materials in dual-ion batteries. *Electrochim Acta* 2022;435:141402. DOI
48. Ba Z, Wang Z, Luo M, et al. Benzoquinone-based polyimide derivatives as high-capacity and stable organic cathodes for lithium-ion batteries. *ACS Appl Mater Interfaces* 2020;12:807-17. DOI
49. Kapaev RR, Scherbakov AG, Shestakov AF, Stevenson KJ, Troshin PA. m-phenylenediamine as a building block for polyimide battery cathode materials. *ACS Appl Energy Mater* 2021;4:4465-72. DOI
50. Kim T, Park B, Lee KM, et al. Hydrothermal synthesis of composition- and morphology-tunable polyimide-based microparticles. *ACS Macro Lett* 2018;7:1480-5. DOI
51. Ham Y, Fritz NJ, Hyun G, et al. 3D periodic polyimide nano-networks for ultrahigh-rate and sustainable energy storage. *Energy Environ Sci* 2021;14:5894-902. DOI
52. Ryu J, Park B, Kang J, et al. Three-dimensional monolithic organic battery electrodes. *ACS Nano* 2019;13:14357-67. DOI
53. Chen L, Li W, Wang Y, Wang C, Xia Y. Polyimide as anode electrode material for rechargeable sodium batteries. *RSC Adv* 2014;4:25369-73. DOI
54. Geng J, Ni Y, Zhu Z, et al. Reversible metal and ligand redox chemistry in two-dimensional iron-organic framework for sustainable lithium-ion batteries. *J Am Chem Soc* 2023;145:1564-71. DOI
55. Yu Z, Huang L, Sun Z, Cai F, Liang M, Luo Z. Designing anthraquinone-based conjugated microporous polymers with dual-ion storage behavior towards high-performance lithium-organic batteries. *J Power Sources* 2022;550:232149. DOI
56. Xiu Y, Mauri A, Dinda S, et al. Anion storage chemistry of organic cathodes for high-energy and high-power density divalent metal batteries. *Angew Chem Int Ed* 2023;62:e202212339. DOI PubMed PMC
57. Zhang Y, Nie P, Xu C, et al. High energy aqueous sodium-ion capacitor enabled by polyimide electrode and high-concentrated electrolyte. *Electrochim Acta* 2018;268:512-9. DOI
58. Wu H, Ye Z, Zhu J, Luo S, Li L, Yuan W. High discharge capacity and ultra-fast-charging sodium dual-ion battery based on insoluble organic polymer anode and concentrated electrolyte. *ACS Appl Mater Interfaces* 2022;14:49774-84. DOI
59. Jiang H, Wei Z, Ma L, et al. An aqueous dual-ion battery cathode of Mn_3O_4 via reversible insertion of nitrate. *Angew Chem Int Ed* 2019;58:5286-91. DOI
60. Zhang F, Wu M, Wang X, et al. Reversible multi-electron redox chemistry of organic salt as anode for high-performance Li-ion/dual-ion batteries. *Chem Eng J* 2023;457:141335. DOI
61. Huang Z, Hou Y, Wang T, et al. Author correction: manipulating anion intercalation enables a high-voltage aqueous dual ion battery. *Nat Commun* 2021;12:4885. DOI PubMed PMC
62. Sun Z, Zhu K, Liu P, Chen X, Li H, Jiao L. Fluorination treatment of conjugated protonated polyanilines for high-performance sodium dual-ion batteries. *Angew Chem Int Ed* 2022;61:e202211866. DOI
63. Mu S, Liu Q, Kidkhunthod P, Zhou X, Wang W, Tang Y. Molecular grafting towards high-fraction active nanodots implanted in N-doped carbon for sodium dual-ion batteries. *Natl Sci Rev* 2021;8:nwaa178. DOI PubMed PMC
64. Wu S, Zhang F, Tang Y. A novel calcium-ion battery based on dual-carbon configuration with high working voltage and long cycling life. *Adv Sci* 2018;5:1701082. DOI
65. Wei C, Gong D, Xie D, Tang Y. The free-standing alloy strategy to improve the electrochemical performance of potassium-based dual-ion batteries. *ACS Energy Lett* 2021;6:4336-44. DOI
66. He F, Zhou Y, Chen X, et al. A bipolar pyridine-functionalized porphyrin with hybrid charge-storage for dual-ion batteries. *Chem Commun* 2023;59:2787-90. DOI
67. Yang K, Liu Q, Zheng Y, Yin H, Zhang S, Tang Y. Locally ordered graphitized carbon cathodes for high-capacity dual-ion batteries. *Angew Chem Int Ed* 2021;60:6326-32. DOI
68. Wang J, Polleux J, Lim J, Dunn B. Pseudocapacitive contributions to electrochemical energy storage in TiO_2 (anatase) nanoparticles. *J Phys Chem C* 2007;111:14925-31. DOI
69. Jiang B, Su Y, Liu R, Sun Z, Wu D. Calcium based all-organic dual-ion batteries with stable low temperature operability. *Small* 2022;18:e2200049. DOI
70. Lu P, Sun Y, Xiang H, Liang X, Yu Y. 3D Amorphous carbon with controlled porous and disordered structures as a high-rate anode material for sodium-ion batteries. *Adv Energy Mater* 2018;8:1702434. DOI
71. Tang B, Fang G, Zhou J, et al. Potassium vanadates with stable structure and fast ion diffusion channel as cathode for rechargeable aqueous zinc-ion batteries. *Nano Energy* 2018;51:579-87. DOI
72. He B, Man P, Zhang Q, et al. All Binder-free electrodes for high-performance wearable aqueous rechargeable sodium-ion batteries. *Nanomicro Lett* 2019;11:101. DOI PubMed PMC
73. Zhou G, An X, Zhou C, Wu Y, Miao Y, Liu T. Highly porous electroactive polyimide-based nanofibrous composite anode for all-organic aqueous ammonium dual-ion batteries. *Compos Commun* 2020;22:100519. DOI

74. Wu H, Hu T, Chang S, Li L, Yuan W. Sodium-based dual-ion battery based on the organic anode and ionic liquid electrolyte. *ACS Appl Mater Interfaces* 2021;13:44254-65. DOI
75. Lei X, Zheng Y, Zhang F, Wang Y, Tang Y. Highly stable magnesium-ion-based dual-ion batteries based on insoluble small-molecule organic anode material. *Energy Stor Mater* 2020;30:34-41. DOI
76. Li Y, Guan Q, Cheng J, Wang B. Flexible high energy density sodium dual-ion battery with long cycle life. *Energy Environ Mater* 2022;5:1285-93. DOI
77. Park S, Yoo J, Chang B, Ahn E. Novel instrumentation in electrochemical impedance spectroscopy and a full description of an electrochemical system. *Pure Appl Chem* 2006;78:1069-80. DOI
78. Yang W, Zhou J, Wang S, et al. Freestanding film made by necklace-like N-doped hollow carbon with hierarchical pores for high-performance potassium-ion storage. *Energy Environ Sci* 2019;12:1605-12. DOI
79. Ma W, Luo L, Huang X, et al. Dihydrophenazine-based conjugated microporous polymer cathodes with enhanced electronic and ionic conductivities for high-performance aluminum dual-ion batteries. *Adv Energy Mater* 2023;13:2203253. DOI
80. Li Z, Liu J, Niu B, Li J, Kang F. A novel graphite-graphite dual ion battery using an $AlCl_3^-$[EMIm]Cl liquid electrolyte. *Small* 2018;14:e1800745. DOI
81. Tao S, Demir B, Baktash A, et al. Solvent-derived fluorinated secondary interphase for reversible Zn-graphite dual-ion batteries. *Angew Chem Int Ed* 2023;62:e202307208. DOI
82. Xiang L, Ou X, Wang X, Zhou Z, Li X, Tang Y. Highly concentrated electrolyte towards enhanced energy density and cycling life of dual-ion battery. *Angew Chem Int Ed* 2020;59:17924-30. DOI
83. Song Z, Zhan H, Zhou Y. Anthraquinone based polymer as high performance cathode material for rechargeable lithium batteries. *Chem Commun* 2009:448-50. DOI PubMed
84. Wu H, Luo S, Li L, Xiao H, Yuan W. A high-capacity dual-ion full battery based on nitrogen-doped carbon nanosphere anode and concentrated electrolyte. *Battery Energy* 2023;2:20230009. DOI
85. Lin R, Ke C, Chen J, Liu S, Wang J. Asymmetric donor-acceptor molecule-regulated core-shell-solvation electrolyte for high-voltage aqueous batteries. *Joule* 2022;6:399-417. DOI
86. Liang Z, Gong D, Shang J, et al. Low volume expansion carbon-coated $Fe_2P_4O_{12}$ anode material for high-performance sodium dual-ion battery. *Energy Stor Mater* 2022;53:331-9. DOI
87. Wu N, Yao W, Song X, et al. A calcium-ion hybrid energy storage device with high capacity and long cycling life under room temperature. *Adv Energy Mater* 2019;9:1803865. DOI
88. Li X, Ou X, Tang Y. 6.0 V high-voltage and concentrated electrolyte toward high energy density K-based dual-graphite battery. *Adv Energy Mater* 2020;10:2002567. DOI